

Atmospheric Correction of Second Generation Ocean

Color Sensors: A Preliminary Algorithm

by

Menghua Wang and Howard R. Gordon

Department of Physics

University of Miami

Coral Gables, FL 33124

Acknowledgement

This work received support from the National Aeronautics and Space Administration under Grant NAGW-273 and Contract NAS5-30911.

Abstract

The algorithm for atmospheric correction of Coastal Zone Color Scanner (CZCS) imagery for retrieval of the water-leaving reflectance is based on the assumption that the Rayleigh-aerosol interaction (ρ_{ra}) can be ignored, i.e., photons that scatter from air molecules never scatter from aerosol particles and vice versa. However, for the new ocean color sensors, e.g., SeaWiFS, the error caused by ignoring the Rayleigh-aerosol interaction can be as much as an order of magnitude larger than their noise equivalent spectral radiance. Therefore, a new algorithm has been developed and is tested here with simulations for several viewing scenarios. It is found that even though the Rayleigh-aerosol interaction term ρ_{ra} is very difficult to model in a realistic situation, the combination of the Rayleigh-aerosol interaction term, ρ_{ra} , and the reflectance due to the aerosol alone, ρ_a , can be accurately determined. The simulations suggest that the error in the retrieved water-leaving reflectance in realistic situations will be within the allowed limits for the next generation ocean color sensors using the new algorithm as long as information regarding the sea surface roughness (wind speed) is available. Finally, a possible implementation of the new algorithm is discussed.

Introduction

The Coastal Zone Color Scanner (CZCS) on Nimbus-7 was a scanning radiometer which viewed the ocean in six co-registered spectral bands, five in the visible and near infrared (443, 520, 550, 670, and 750 nm, labeled Bands 1, 2, 3, 4, and 5, respectively) and one in the thermal infrared (10.5 – 12.5 μ m, Band 6). The purpose of the CZCS was to provide estimates of the near-surface concentration of phytoplankton pigments by measuring the radiance backscattered out of the water.¹⁻³ The next generation ocean color sensors, such as SeaWiFS⁴ and MODIS^{5,6} on EOS will have a radiometric sensitivity (through increased signal to noise and smaller quantization interval) that is superior to CZCS. They also will be equipped with additional spectral bands, e.g., a band near 400 nm to separate the detrital and viable phytoplankton signals, and 765 and 865 nm bands to aid in atmospheric correction. Our goal is to refine the CZCS atmospheric correction algorithm⁷⁻¹³ to utilize fully the new spectral bands and the increased sensitivity in order to improve the accuracy of the pigment retrieval.

In earlier papers^{14,15} we simulated the influence of wind-induced sea surface roughness on the quality of the retrieval of the water-leaving radiances from an ocean color sensor when a CZCS-type algorithm, which assumes a *flat* ocean, is used. We reached three significant conclusions for situations in which there is no direct sun glitter in the image (either a large solar zenith angle or the sensor tilted away from the specular image of the sun). First, the error induced by ignoring the surface roughness is usually $\lesssim 1$ CZCS digital count for wind speeds up to ≈ 17 m/s, and therefore can be ignored for that sensor. Next, the roughness-induced error is much more strongly dependent on the wind speed than on the shadowing of one wave by another, suggesting that surface effects can be adequately dealt with without a precise knowledge of wave shadowing. Finally, the error induced by ignoring the Rayleigh-aerosol interaction is usually larger than that caused by ignoring the surface roughness, suggesting that, in refining algorithms for future sensors, more effort should be placed on dealing with the Rayleigh-aerosol interaction than on the roughness of the sea surface. In the present paper, we present a preliminary algorithm for the atmospheric correction of the

more-sensitive SeaWiFS instrument. In contrast to CZCS, it will be shown that knowledge of the surface roughness is an important ingredient in the SeaWiFS algorithm.

We begin by showing that the standard CZCS algorithm yields unacceptable results with SeaWiFS. The ideas of Gordon and Castaño¹⁶ are then expanded to develop a technique for including the Rayleigh-aerosol interaction in the formalism. Next, a refined algorithm is proposed, and tested through very precise radiative transfer simulations. Finally, strategies for implementing the algorithm are discussed.

CZCS Algorithm Error and Required Accuracy for New Sensors

We begin with the definition of reflectance ρ :

$$\rho = \pi L / F_0 \cos \theta_0, \quad (1)$$

where L is the upward radiance in the given viewing direction, F_0 is the extraterrestrial solar irradiance, and θ_0 is the solar zenith angle. With this normalization for L , ρ determined at the top of the atmosphere would be the albedo of the ocean-atmosphere system if L were independent of the viewing angle. Because it is often more convenient to work with dimensionless reflectance (ρ) rather than radiance (L), and because the new sensors may be calibrated in reflectance instead of radiance, we shall abandon L in favor of ρ in this paper. Note, however, that given F_0 , the transformation from one to the other is trivial. We can write the total reflectance, at a wavelength λ , measured at the top of the atmosphere as

$$\rho_t(\lambda) = \rho_r(\lambda) + \rho_a(\lambda) + \rho_{ra}(\lambda) + \rho_g(\lambda) + t\rho_w(\lambda), \quad (2)$$

where ρ_r is the reflectance resulting from multiple scattering by air molecules (Rayleigh scattering) in the absence of aerosols, ρ_a is the reflectance resulting from multiple scattering by aerosols in the absence of the air, ρ_{ra} is the interaction term between molecules and aerosols,¹⁷ ρ_g is the reflectance of the direct solar beam, i.e., photons that are specular reflected from the (rough) ocean surface, and ρ_w is the water-leaving reflectance. The ρ_g term in the above equation is generally ignored

because ocean color sensors are equipped with a provision for tilting the scan plane away from the specular image of the sun. The term ρ_{ra} accounts for the interaction between Rayleigh and aerosol scattering, e.g., photons first scattered by the air then scattered by aerosols, or photons first scattered by aerosols then air, etc. This term is zero in the single scattering case, in which photons are only scattered once, and can be ignored as long as the amount of multiple scattering is small, i.e., at small Rayleigh and aerosol optical thicknesses. In the case of CZCS, the interaction term can be virtually ignored since CZCS does not possess sufficiently high radiometric sensitivity. The new ocean color sensors, e.g., SeaWiFS, however, will have higher radiometric sensitivity, and ρ_{ra} must be considered.

Ignoring the term of ρ_g , we can write Eq. (2) as

$$\rho_t(\lambda) = \rho_r(\lambda) + \rho_a(\lambda) + \rho_{ra}(\lambda) + t\rho_w(\lambda). \quad (3)$$

The purpose of atmospheric correction is to retrieve ρ_w from the above equation. In principle the reflectances $\rho_r + \rho_a + \rho_{ra}$ could be removed if the concentration and optical properties of the aerosol were known throughout an image. The aerosol, however, is highly variable, and, unlike the Rayleigh scattering component ρ_r , the effects of $\rho_a + \rho_{ra}$ on the imagery cannot be predicted a priori. The CZCS atmospheric correction algorithm is based on the fact that the term ρ_{ra} can

Table 1: Error ($\Delta\rho$) at 443 nm in the CZCS atmospheric correction algorithm at $\theta_0 = 60^\circ$.

σ	$\tau_a = 0.2$		$\tau_a = 0.4$	
	Center	Edge	Center	Edge
0	0.0014	0.0026	0.0024	0.0052
0.2	0.0010	0.0023	0.0020	0.0045
0.3	0.0010	0.0021	0.0020	0.0041

be ignored.^{8,9,11-13,18} Given the sea surface roughness (wind speed) and a model of the aerosol (its phase function) the error caused in using the CZCS correction algorithm can be estimated. Using the computations of Gordon and Wang^{14,15} this error is shown in Table 1 for a solar zenith angle (θ_0) of 60° at a wavelength of 443 nm. In the table the terms “Center” and “Edge” refer to the center and the edge of the CZCS scan, respectively. τ_a is the aerosol optical thickness and

is assumed independent of λ in the simulation. σ^2 is the variance of the Cox and Munk¹⁹ surface slope distribution ignoring the wind direction. It is related to the wind speed W (m/s) measured 10 m above the sea surface. Nakajima and Tanaka²⁰ summarize the results of several investigators by

$$\sigma^2 = 0.00534 W.$$

From Table 1 we can see that the error using the CZCS atmospheric correction algorithm, for $\theta_0 = 60^\circ$, $\sigma = 0.2$, and $\tau_a = 0.2$, at the scan edge $\Delta\rho$ is ~ 0.0023 , while for $\tau_a = 0.4$ it is ~ 0.0045 . Table 2 gives the Noise Equivalent Reflectance ($NE\Delta\rho$) proposed for SeaWiFS at $\theta_0 = 60^\circ$. In Table 2, ρ_{max} is the saturation reflectance, ρ_w is the water-leaving reflectance corresponding to a chlorophyll concentration of ~ 0.03 mg/m³, and ρ_t is the reflectance at which the $NE\Delta\rho$ is specified. ρ_t was determined at the scan edge using an atmospheric model with $\theta_0 = 60^\circ$. From this table we see that the $NE\Delta\rho$ is ~ 0.0007 for $\lambda = 412$ nm and ~ 0.0004 for $\lambda = 443$ nm at $\theta_0 = 60^\circ$. Thus, in order to utilize the full sensitivity of SeaWiFS in this viewing geometry, the error ($\Delta\rho$) in atmospheric correction should be $\lesssim 0.0004$ at 443 nm. Obviously, the CZCS atmospheric correction algorithm is not good enough even for lower values of τ_a , and we need a new scheme for atmospheric correction of SeaWiFS. If the viewing geometry changes, ρ_t will also change, and this in turn will change the $NE\Delta\rho$ as well. To estimate $NE\Delta\rho$ in other geometries we assume that the noise equivalent spectral radiance, $NE\Delta L$, is related to the radiance, L_t , through $NE\Delta L \propto (L_t)^p$ where $0.5 < p < 1$. (If the sensor noise is dominated by shot noise²¹ in the detectors, $p = 0.5$.) L_t is computed for other geometries using the same atmospheric model used for ρ_t in Table 1, enabling $NE\Delta\rho$ to be estimated. Figure 1 provides the $NE\Delta\rho$ at the scan edge as a function of θ_0 for $p = 0.5$ and 1.0. Note that the precise value of p is not important and that the $NE\Delta\rho$ decreases as θ_0 decreases. In what follows, we will adopt the smaller $NE\Delta\rho$ in Figure 1 (worst case) at each θ_0 as the upper limit to the allowed error in the atmospheric correction, i.e., our goal is that the error in the atmosphere correction algorithm $\lesssim NE\Delta\rho$.

To extract ρ_w from Eq. (3) we need to estimate ρ_r , ρ_a and ρ_{ra} . The Rayleigh reflectance can be computed knowing the wavelength, the surface pressure, the total Ozone concentration, and the sea surface roughness (see Gordon, Brown and Evans¹³ for the details when $\sigma = 0$, and Gordon and

Table 2: SeaWiFS Performance for $\theta_0 = 60^\circ$ at the Scan Edge

Band	λ (nm)	ρ_{max}	ρ_w	ρ_t	NE $\Delta\rho$
1	402-422	0.50	0.040	0.34	0.00068
2	433-453	0.46	0.038	0.29	0.00043
3	480-500	0.36	0.024	0.23	0.00034
4	510-530	0.30	0.0096	0.19	0.00031
5	555-575	0.25	0.0040	0.154	0.00027
6	655-675	0.17	0.0004	0.105	0.00023
7	745-785	0.15	-	0.081	0.00018
8	845-885	0.13	-	0.069	0.00015

Wang¹⁴ when $\sigma \neq 0$). We have found that rather than trying to estimate ρ_a and ρ_{ra} separately, it is easier to estimate their sum, $\rho_a + \rho_{ra}$. From Eq. (3), we have

$$\rho_a(\lambda) + \rho_{ra}(\lambda) = \rho_t(\lambda) - \rho_r(\lambda) - t\rho_w(\lambda). \quad (4)$$

For the purpose of developing the algorithm, we let $\rho_w = 0$, and the above equation then becomes

$$\rho_a(\lambda) + \rho_{ra}(\lambda) = \rho_t(\lambda) - \rho_r(\lambda). \quad (5)$$

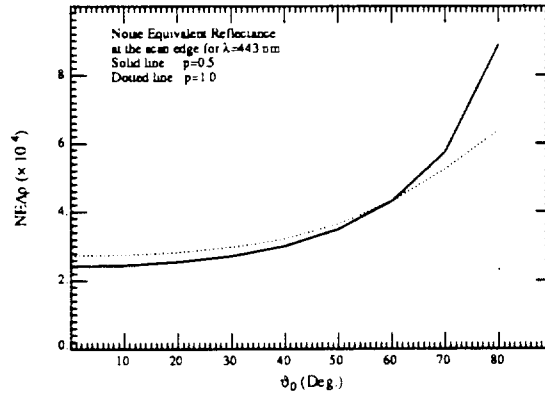


Figure 1. NE $\Delta\rho$ as a function of θ_0 at the scan edge for SeaWiFS. The solid and dotted lines are, respectively, for $p = 0.5$ and $p = 1.0$.

A Proposed Algorithm for New Sensors

Gordon and Castaño¹⁶ found that there exists a very simple relation between $\rho_a(\lambda) + \rho_{ra}(\lambda)$ and $\rho_{as}(\lambda)$, where $\rho_{as}(\lambda)$ is the aerosol reflectance in the *single scattering* and *flat ocean* approximations. If θ_0 and ϕ_0 are, respectively, the zenith and azimuth angles of a vector from the point on the sea surface under examination (the pixel) to the sun, and θ and ϕ are zenith and azimuth angles of a vector from the pixel to the sensor, ρ_{as} is given by

$$\rho_{as}(\lambda) = \omega_a(\lambda)\tau_a(\lambda)p_a(\theta, \theta_0, \lambda)/4 \cos \theta \cos \theta_0, \quad (6)$$

where

$$p_a(\theta, \theta_0, \lambda) = P_a(\theta_-, \lambda) + (\varrho(\theta) + \varrho(\theta_0))P_a(\theta_+, \lambda),$$

$$\cos \theta_{\pm} = \pm \cos \theta_0 \cos \theta - \sin \theta_0 \sin \theta \cos(\phi - \phi_0),$$

and $\varrho(\theta)$ is the Fresnel reflectance of the interface for an incident angle θ . In what follows we take $\phi_0 = 0$. Gordon and Castaño found that for $\lambda = 670$ nm, $\rho_a + \rho_{ra}$ was *linearly* related to ρ_{as} . Here, the relationship is developed at other wavelengths and will be used to find a way to correctly retrieve the term $\rho_a(\lambda) + \rho_{ra}(\lambda)$ within the allowed error. Simulations employing *scalar* radiative transfer theory are used to relate $\rho_a + \rho_{ra}$ to ρ_{as} . In order to carry out the simulations, a model of the vertical structure of the atmosphere is needed. Usually, $\sim 90\%$ of aerosol is confined to a layer of 2-km thickness near the sea surface with $\sim 80\%$ of Rayleigh scattering molecules above the aerosol.¹² Thus, it is reasonable to simplify the scattering atmosphere as a two-layer model with molecules above the aerosols. Following Gordon and Castaño,¹² the simulations use three different aerosol phase functions (Figure 1): one that roughly approximates the marine aerosol phase functions given by Quenzel and Kastner;²² one that approximated the Diermendjian Haze L distribution²³ with a refractive index of 1.55 used to represent continental-type aerosols; and one that approximates the Diermendjian Haze C distribution with a slope parameter $\nu = 3.5$ and a refractive index of 1.50 (also continental in nature). The phase functions are approximate in the sense that they have been fit to the two-term Henyey-Greenstein phase function.^{12,24} Three wind-speeds ($\sigma = 0, 0.2, \text{ and } 0.3$

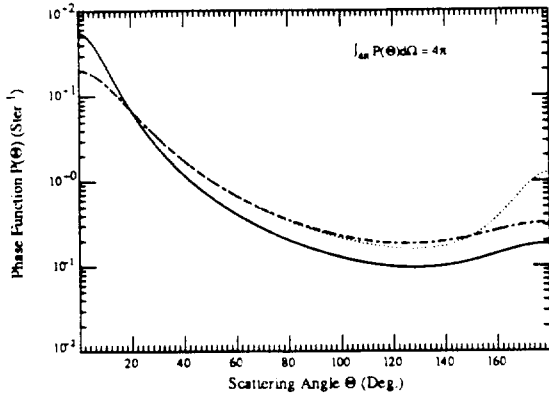


Figure 2. Aerosol phase functions used in the study: Dotted line, Haze L; Dashed line, Haze C; Solid line, Marine aerosol model.

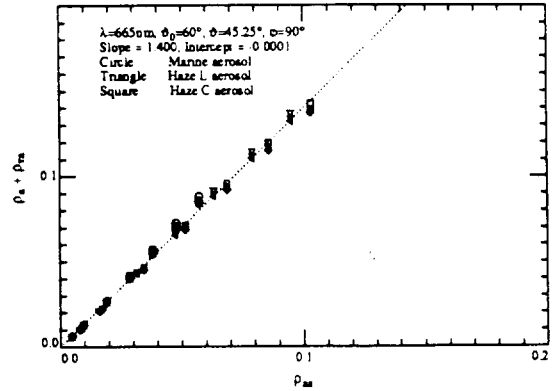


Figure 3. $\rho_a + \rho_{ra}$ as a function of ρ_{as} for $\theta_0 = 60^\circ$, $\theta = 45.25^\circ$, and $\phi = 90^\circ$ at $\lambda = 665$ nm.

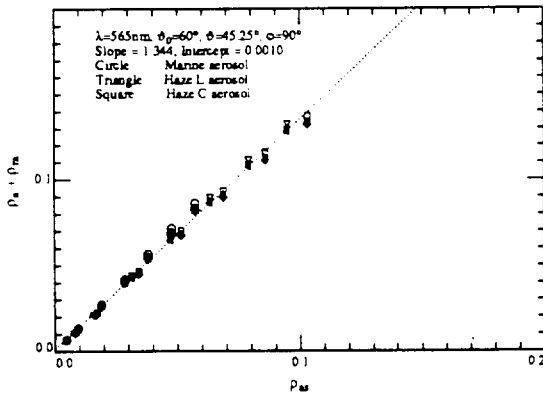


Figure 4. $\rho_a + \rho_{ra}$ as a function of ρ_{as} for $\theta_0 = 60^\circ$, $\theta = 45.25^\circ$, and $\phi = 90^\circ$ at $\lambda = 565$ nm.

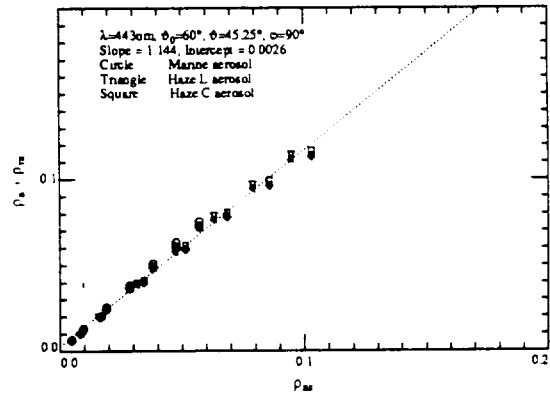


Figure 5. $\rho_a + \rho_{ra}$ as a function of ρ_{as} for $\theta_0 = 60^\circ$, $\theta = 45.25^\circ$, and $\phi = 90^\circ$ at $\lambda = 443$ nm.

or $W=0, 7.5,$ and 16.9 m/s) are used in the computations. The simulations were carried out near the CZCS wavelengths for $\lambda = 443, 565$ and 665 nm, which are denoted by $\lambda_1, \lambda_3,$ and $\lambda_4,$ and for values of θ_0 from 0° to 80° with steps of 10° . Figures 3-5 provide the resulting $\rho_a(\lambda) + \rho_{ra}(\lambda)$ vs. $\rho_{as}(\lambda)$ relationships at the scan edge for $\theta_0 = 60^\circ$ and $\Delta\phi = 90^\circ$. The figures include all the aerosol models (Haze L, Haze C and Marine aerosols) and all surface roughnesses ($\sigma = 0, 0.2,$ and 0.3). For the rough surface cases the bidirectional shadowing factor^{14,15} has been used. The aerosol optical thicknesses τ_a for these figures are $0.05, 0.1, 0.2, 0.3, 0.4, 0.5,$ and 0.6 . For each group of symbols, the top one refers to a flat sea surface, i.e., the empty circle (\circ), empty triangular (Δ)

and empty square (\square) refer to flat sea surface ($\sigma = 0$) for Marine, Haze L and Haze C aerosols, respectively. The others refer to cases with a rough sea surface. The straight line is computed using least-squares. We can see from Figures 3-5 that the slope of the straight line decreases from large wavelength to small wavelength, which implies that the interaction term ρ_{ra} is usually negative and its magnitude increases with decreasing wavelength (increasing τ_r). The most striking feature of Figures 3-5 is the similarity of the distribution of the points around the straight line for the three different wavelengths. For example, the largest $\rho_a + \rho_{ra}$ in the figures corresponds to the Haze C aerosol (squares). The positions of the empty squares (\square) (or solid squares) of the largest $\rho_a + \rho_{ra}$ around the straight line in Figures 3-5 are similar, i.e., they fall *below* the line. This similarity can also be observed for other sets of points on the figures, suggesting that if we can estimate ρ_{as} at 443 nm by extrapolation of ρ_{as} from $\lambda = 665$ and 565 nm, then it may be possible to retrieve the $\rho_a + \rho_{ra}$ accurately at 443 nm from the straight line. Based on this idea, a new algorithm of the atmospheric correction is proposed and tested with simulations. The algorithm consists of five steps delineated below.

(1) Calculate the slope (S) and intercept (I) of the straight line of $\rho_t(\lambda) - \rho_r(\lambda)$ vs. $\rho_{as}(\lambda)$ for each wavelength and the given geometry, i.e., for all θ , θ_0 , ϕ , λ , from simulations. This single line should include all of the aerosol models, since in practice the optical properties of aerosol are unknown. If the wind speed is known, the correct value should be used, otherwise simulations should be carried out for a range of wind speeds, all of which should be included in the determination of the S and I . It is important to note here that since $\rho_w = 0$ in the simulations, $\rho_t - \rho_r$ is really $\rho_a + \rho_{ra}$ (Eq. (5)). Henceforth we assume S and I are known for all wavelengths (λ), sun angles (θ_0), viewing angles (θ), and azimuth angles (ϕ) of interest.

(2) Use the measured value of $\rho_t(\lambda)$ at the longer wavelengths, where in nature $\rho_w \simeq 0$, or is known, to estimate $\rho_{as}(\lambda)$ through

$$\rho_t(\lambda) - \rho_r(\lambda) - t\rho_w(\lambda) = I(\lambda) + S(\lambda)\rho_{as}(\lambda), \quad (7)$$

where $I(\lambda)$ and $S(\lambda)$ are known from (1) for the given geometry.

(3) Determine $\rho_{as}(\lambda)$ at other wavelengths of interest for ocean color, by using a CZCS-type correction algorithm. For example, suppose we want to find $\rho_{as}(\lambda_1)$ from $\rho_{as}(\lambda_3)$ and $\rho_{as}(\lambda_4)$, we first define

$$\frac{\rho_{as}(\lambda_i)}{\rho_{as}(\lambda_j)} = \frac{\omega_a(\lambda_i)\tau_a(\lambda_i)p_a(\theta, \theta_0, \lambda_i)}{\omega_a(\lambda_j)\tau_a(\lambda_j)p_a(\theta, \theta_0, \lambda_j)} \equiv \epsilon(\lambda_i, \lambda_j). \quad (8)$$

We note that, unlike the ϵ -factors in the standard CZCS algorithm,¹² all multiple scattering effects have been removed from the ϵ -factors defined by Eq. (8). Thus, this ϵ is truly independent of the aerosol concentration and varies in space only to the extent that P_a depends on λ and the aerosol *type* varies in space. We then compute $\epsilon(\lambda_3, \lambda_4)$ and $\epsilon(\lambda_1, \lambda_4)$ from the above equation ($\rho_{as}(\lambda_3)$ and $\rho_{as}(\lambda_4)$ are known because $\rho_w(\lambda_3)$ and $\rho_w(\lambda_4)$ are assumed to be known) and extrapolate to find $\epsilon(\lambda, \lambda_4)$ for any λ by assuming that

$$\epsilon(\lambda, \lambda_4) = \left(\frac{\lambda_4}{\lambda}\right)^n. \quad (9)$$

Finally, $\rho_{as}(\lambda_1) = \epsilon(\lambda_1, \lambda_4)\rho_{as}(\lambda_4)$.

(4) The value of $\rho_a(\lambda) + \rho_{ra}(\lambda)$ at λ_1 is obtained from $\rho_a(\lambda_1) + \rho_{ra}(\lambda_1) = I(\lambda_1) + S(\lambda_1)\rho_{as}(\lambda_1)$.

(5) Finally, the total atmospheric reflectance is obtained by adding the above component to the computed Rayleigh scattering component, i.e.,

$$t(\lambda_1)\rho_w(\lambda_1) = \underbrace{\rho_t(\lambda_1)}_{\text{Measured}} - \underbrace{\rho_r(\lambda_1)}_{\text{Calculated}} - \underbrace{(\rho_a(\lambda_1) + \rho_{ra}(\lambda_1))}_{\text{Estimated}}.$$

We note that extrapolation of $\epsilon(\lambda_3, \lambda_4)$ to other wavelengths (Eq. (9)) plays a central role in this algorithm. Although the simple form chosen here should be a good approximation over the relatively narrow spectral range of CZCS (443 – 670 nm), it may not be adequate for the larger SeaWiFS range (412 – 865 nm).

Preliminary Simulations

We have performed simulations using codes developed for our earlier work,^{14,15} to test the efficacy of this algorithm in estimating $\rho_w(\lambda_1)$ given $\rho_w(\lambda_3)$ and $\rho_w(\lambda_4)$, i.e., being given ρ_w at 565

and 665 nm and being asked to estimate ρ_w in the blue. In the case of CZCS this would be an example of estimating the pigment concentration ²⁵ (C) in clear water,¹⁸ i.e., pigment concentration $\lesssim 0.25$ mg/m³. For C in this range, the water leaving reflectance (radiance) is known in the green and red, and its determination in the blue leads to an estimate of C . Eq. (3) in this kind of situation reads

$$t(\lambda_1)\rho_w(\lambda_1) = \rho_t^{(m)}(\lambda_1) - \rho_r(\lambda_1) - \rho_a(\lambda_1) - \rho_{ra}(\lambda_1), \quad (10)$$

where $\rho_t^{(m)}(\lambda_1)$ is the total reflectance measured (“ m ”) by the sensor. The reflectances $\rho_r(\lambda_1)$ and $\rho_a(\lambda_1) + \rho_{ra}(\lambda_1)$ must be computed to find $\rho_w(\lambda_1)$. The computation of $\rho_r(\lambda_1)$ requires an assumption regarding the roughness of the sea surface, e.g., that the surface is flat. Since the assumption is not necessarily correct, we indicate the resulting ρ_r by $\rho_r^{(c)}$, the superscript “ c ” indicating “computed”. The value of $\rho_a(\lambda_1) + \rho_{ra}(\lambda_1)$ is obtained by using the algorithm discussed in the previous section. Then the retrieved value $\rho_w^{(c)}(\lambda_1)$ is given by

$$t(\lambda_1)\rho_w^{(c)}(\lambda_1) = \rho_t^{(m)}(\lambda_1) - \rho_r^{(c)}(\lambda_1) - [\rho_a(\lambda_1) + \rho_{ra}(\lambda_1)]^{(c)}, \quad (11)$$

and the error in $t(\lambda_1)\rho_w(\lambda_1)$ is $\Delta\rho(\lambda_1) \equiv t(\lambda_1)[\rho_w^{(c)}(\lambda_1) - \rho_w(\lambda_1)]$. In our simulation of $\rho_t^{(m)}(\lambda_1)$, $\rho_w(\lambda_1)$ is taken to be zero, so $\Delta\rho(\lambda_1) = t(\lambda_1)\rho_w^{(c)}(\lambda_1)$.

The computations have been carried out for the CZCS-like scan, at the scan center and scan edge. The scan azimuth is set normal to the azimuth of the solar beam, i.e., CZCS, and most likely SeaWiFS, geometry. Figures 6-15 provide the examples of error $\Delta\rho(\lambda_1)$ at the scan edge for the different scenarios. Figure 6 provides an example of the error $\Delta\rho(\lambda_1)$ for a Marine aerosol ($\tau_a(665) = 0.4$) in a situation in which the surface roughness is unknown. The values of $S(\lambda)$ and $I(\lambda)$ used for this figure are computed by including all of the wind-speeds ($\sigma = 0, 0.2$ and 0.3), all of the aerosol models (Marine, Haze L and Haze C aerosols) and all of the τ_a values (0.05, 0.1, 0.2, 0.3, 0.4, 0.5, and 0.6) used in the simulations. The aerosol phase functions are assumed to be independent of wavelength, and the aerosols are assumed to be nonabsorbing ($\omega_a = 1$). In general we let $\tau_a(\lambda) \propto \lambda^{-n_a}$. With a nonabsorbing, wavelength-independent aerosol phase function, $n_a = n$ in Eq. (9). In the particular case in Figure 6, $n_a = 0$, i.e., $\tau_a \propto \lambda^{-0}$. The x -axis is the zenith angle of the solar beam, which is from 0°–80° in steps of 10°. The solid circles (●) refer to the case where

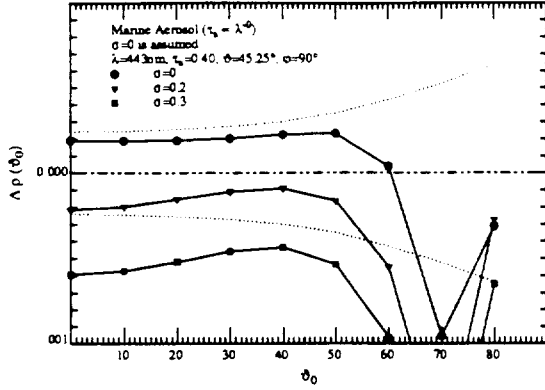


Figure 6. Error in the retrieved reflectance at the scan edge as a function of the sun angle for a Marine aerosol with $\tau_a(\lambda_4) = 0.4$ and $n_a = 0$. The surface roughness is unknown.

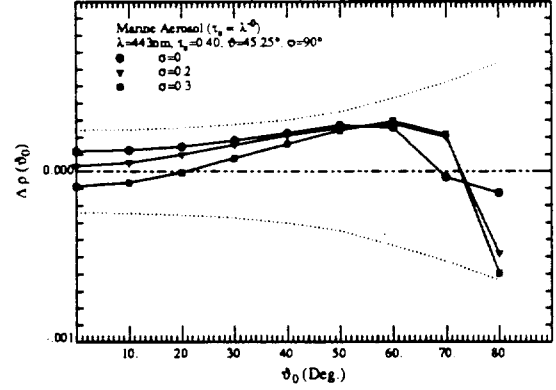


Figure 7. Error in the retrieved reflectance at the scan edge as a function of the sun angle for a Marine aerosol with $\tau_a(\lambda_4) = 0.4$ and $n_a = 0$. The surface roughness is known.

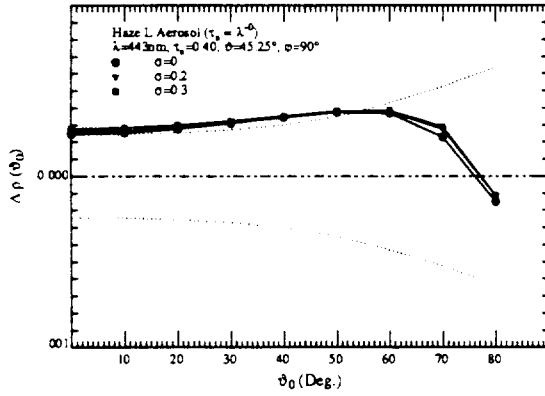


Figure 8. Error in the retrieved reflectance at the scan edge as a function of the sun angle for a Haze L aerosol with $\tau_a(\lambda_4) = 0.4$ and $n_a = 0$. The surface roughness is known.

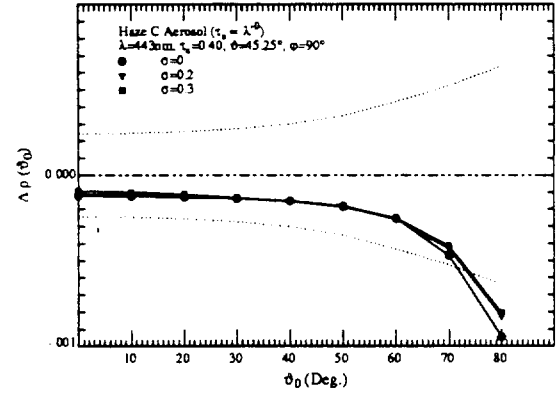


Figure 9. Error in the retrieved reflectance at the scan edge as a function of the sun angle for a Haze C aerosol with $\tau_a(\lambda_4) = 0.4$ and $n_a = 0$. The surface roughness is known.

the ocean is assumed to be flat for the computation of $\rho_r(\lambda_i)$ and it actually is flat. The error in this case is partially due to the fact that $\sigma = 0.2$ and $\sigma = 0.3$ are included in the computation of $S(\lambda)$ and $I(\lambda)$. The solid triangles (\blacktriangledown) and squares (\blacksquare) refer to the cases in which the actual wind speed is 7.5 m/s ($\sigma = 0.2$) and 16.9 m/s ($\sigma = 0.3$), respectively, but it is assumed to be zero ($\sigma = 0$) for the computation of $\rho_r(\lambda_i)$. The additional error in these two cases is mainly from the assumption that the surface is flat (in the ρ_r computation) in the presence of wind-induced surface roughness. The dotted lines in this and the rest of the figures correspond to the worst-case $NE\Delta\rho$

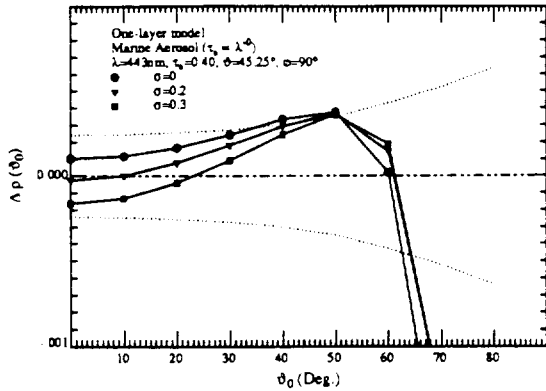


Figure 10. Error in the retrieved reflectance at the scan edge as a function of the sun angle for a Marine aerosol with $\tau_a(\lambda_4) = 0.4$ and $n_a = 0$. The surface roughness is known, but the vertical structure of atmosphere is unknown.

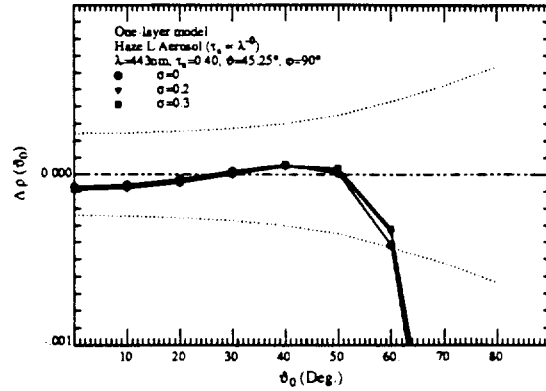


Figure 11. Error in the retrieved reflectance at the scan edge as a function of the sun angle for a Haze L aerosol with $\tau_a(\lambda_4) = 0.4$ and $n_a = 0$. The surface roughness is known, but the vertical structure of atmosphere is unknown.

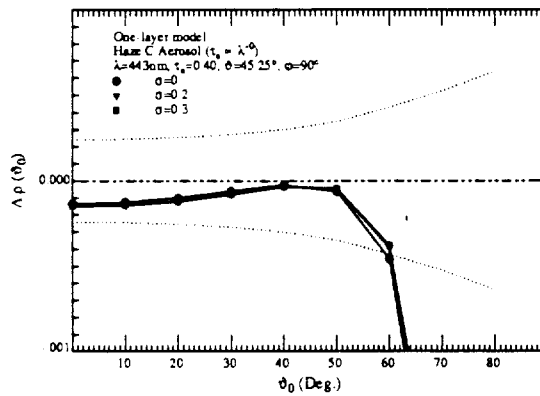


Figure 12. Error in the retrieved reflectance at the scan edge as a function of the sun angle for a Haze C aerosol with $\tau_a(\lambda_4) = 0.4$ and $n_a = 0$. The surface roughness is known, but the vertical structure of atmosphere is unknown.

in Figure 1. When $\Delta\rho$ falls between the dotted lines, the error in the correction algorithm is $<$ the estimated sensor noise. Note that over the range $0 \lesssim \theta_0 \lesssim 60^\circ$, $\Delta\rho$ is very close to that required for SeaWiFS even though the wind speed is unknown.

Figure 7 is similar to Figure 6 except that now the surface roughness (wind speed) is assumed to be known. In this case $S(\lambda)$ and $I(\lambda)$, as well as ρ_r , are computed using only simulations with the *correct* surface roughness. Note the significant reduction in $\Delta\rho(\lambda_1)$ when the wind speed is

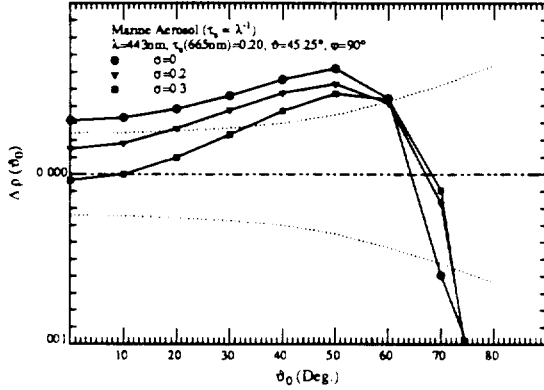


Figure 13. Error in the retrieved reflectance at the scan edge as a function of the sun angle for a Marine aerosol with $\tau_a(\lambda_4) = 0.2$ and $n_a = 1$. The surface roughness is known.

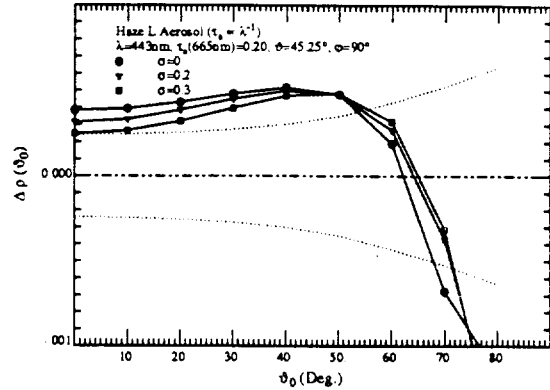


Figure 14. Error in the retrieved reflectance at the scan edge as a function of the sun angle for a Haze L aerosol with $\tau_a(\lambda_4) = 0.2$ and $n_a = 1$. The surface roughness is known.

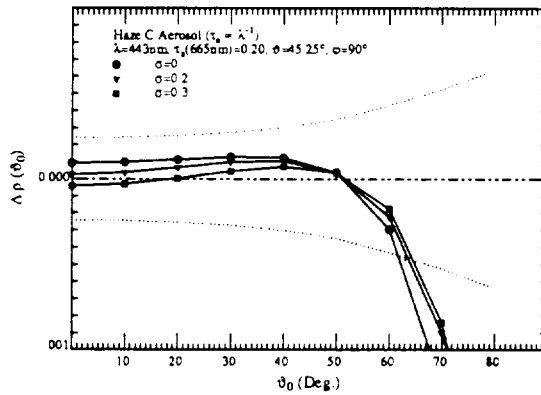


Figure 15. Error in the retrieved reflectance at the scan edge as a function of the sun angle for a Haze C aerosol with $\tau_a(\lambda_4) = 0.2$ and $n_a = 1$. The surface roughness is known.

provided. Now $\Delta\rho$ is less than the SeaWiFS NE $\Delta\rho$ for all $\theta_0 \lesssim 80^\circ$. Figures 8-9 are for cases with a Haze L and Haze C aerosol phase function, respectively. These results are very encouraging. The maximum error $\Delta\rho$ is ~ 0.0004 up to $\theta_0 = 70^\circ$, and no a priori information regarding the aerosol is assumed.

In the examples thus far, the vertical structure of the atmosphere in the simulations has been the same as that used in the initial computation of $S(\lambda)$ and $I(\lambda)$. Figures 10-12 provide examples of the error $\Delta\rho(\lambda_1)$ for the situation in which the vertical structure of the atmosphere is significantly

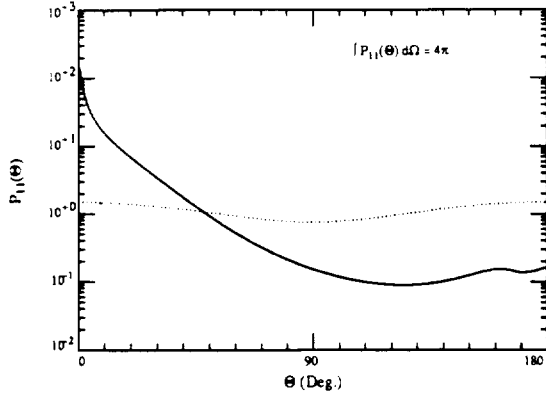


Figure 16a. P_{11} element of the scattering matrix for aerosols (solid line) and molecules (dotted line) as a function of the scattering angle. $P_{22} = P_{11}$.

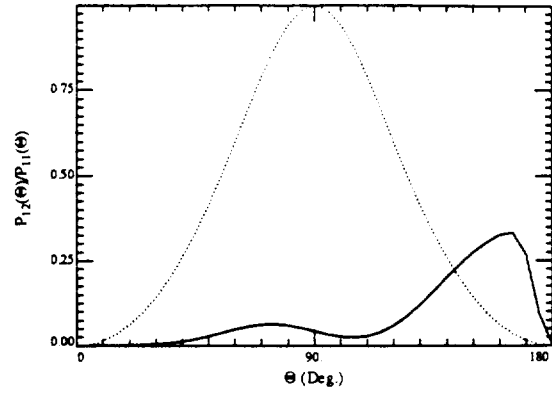


Figure 16b. P_{12} element of the scattering matrix for aerosols (solid line) and $-P_{12}$ for molecules (dotted line) as a function of the scattering angle. $P_{21} = P_{12}$.

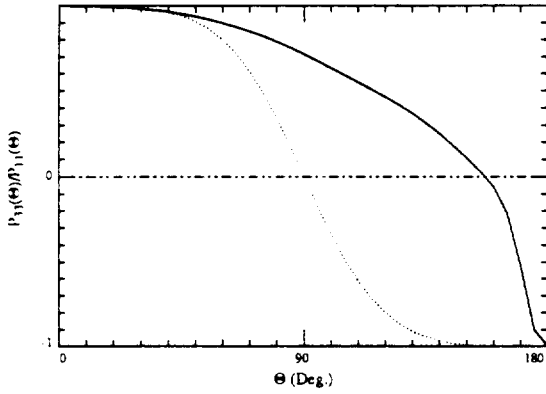


Figure 16c. P_{33} element of the scattering matrix for aerosols (solid line) and molecules (dotted line) as a function of the scattering angle. $P_{44} = P_{33}$.

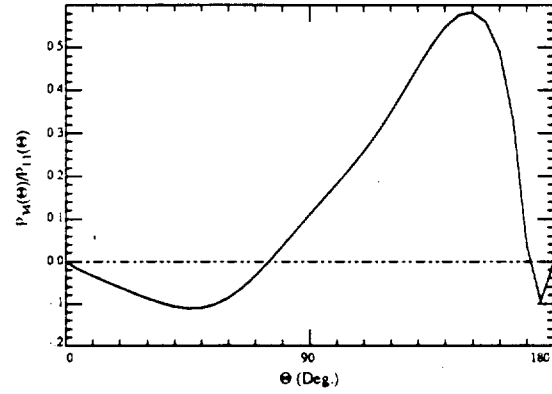


Figure 16d. P_{34} element of the scattering matrix for aerosols (solid line) and molecules ($P_{34} = 0$) as a function of the scattering angle. $P_{43} = -P_{34}$.

different from that used to determine S and I . In these figures, the vertical structure is a uniform mixture of molecules and aerosols, i.e., the $\rho_t^{(m)}(\lambda_i)$ is simulated as a uniform mixture of molecules and aerosols. The $S(\lambda)$ and $I(\lambda)$, however, are still taken from the two-layer atmosphere models. The surface roughness is assumed to be known. Obviously, only a small error arises from the incorrect assumption regarding the vertical structure as long as $\theta_0 \leq 60^\circ$.

Simulations have also been carried out with an aerosol model for which $n_a = 1$ and $\tau_a(665) = 0.2$ (Figures 13-15). Obviously, the error $\Delta\rho(\lambda_1)$ in the $n_a = 1$ case is larger than the case of

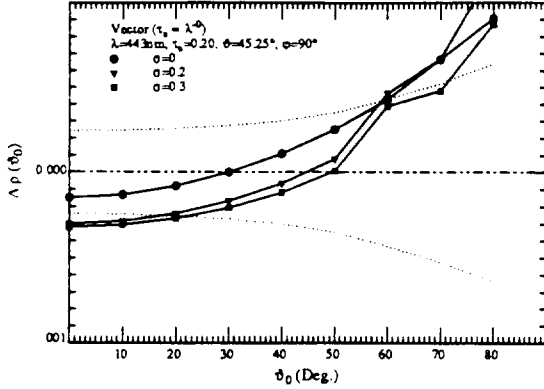


Figure 17. Error in the retrieved reflectance including polarization at the scan edge as a function of the sun angle for $\tau_a(\lambda_4) = 0.2$ and $n_a = 0$. The surface roughness is known.

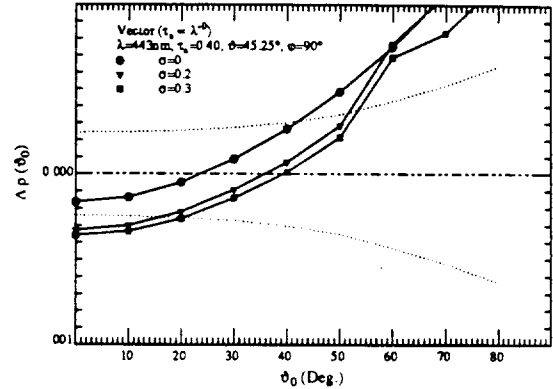


Figure 18. Error in the retrieved reflectance including polarization at the scan edge as a function of the sun angle for $\tau_a(\lambda_4) = 0.4$ and $n_a = 0$. The surface roughness is known.

$n_a = 0$. The reason is that the whole algorithm is based on the similarity of the distribution of points in $\rho_t - \rho_r$ vs. ρ_{as} around the straight line for different wavelengths (Figures 3-5). Usually, the points near the same value of ρ_{as} for different wavelengths are most similar. When $n_a = 1$, the values of $\rho_{as}(\lambda)$ differ considerably, and the similarity is weakened. Therefore, the error $\Delta\rho(\lambda_1)$ in case of $n_a \neq 0$ is larger.

Thus far, polarization has been ignored in all of the computations; however, it is known that using the scalar radiative transfer equation (SRTE) instead of the exact radiative transfer equation (ERTE) can result in significant errors in the computed radiance.^{13,26} Thus, to simulate the radiance measured by the ocean color sensor *correctly* we must use the ERTE which is computationally much more time consuming. Separate simulations have been carried out to illustrate the performance of the algorithm when polarization is included. In these simulations, the aerosol phase matrix used in the ERTE was computed with Mie theory using the Quenzel and Kastner²² marine aerosol model corresponding to a relative humidity of 70%. The nonzero elements of phase matrix $P(\Theta)$ for both aerosol and Rayleigh scattering are shown in Figures 16a-d for $\lambda = 443$ nm. The same aerosol phase matrix was used for all three wavelengths. Also, it was assumed that τ_a was independent of λ , and that the aerosol was nonabsorbing. We note that these assumptions are not all compatible, i.e, the Quenzel and Kastner marine aerosol model yields an aerosol that is slightly absorbing and a phase matrix and aerosol optical thickness that depend weakly on wavelength. However, our

aerosol model does provide parameters that are *realistic*, and this is all that is required for the present analysis. Figures 17 and 18 give the error in $t\rho_w$ for simulations in which the aerosol optical thickness at 665 nm is taken to be 0.2 and 0.4, respectively. In these figures, $S(\lambda)$ and $I(\lambda)$ are *still* computed using the SRTE and the two-layer atmosphere, while the $\rho_t^{(m)}(\lambda_i)$ and $\rho_r^{(c)}(\lambda_i)$ are simulated using the ERTE. The results show that the algorithm performs well even when the radiances are computed correctly (including polarization) and also reveal that using the SRTE-computed slope and intercept does not seem to introduce additional errors that are significant for even relatively large values of τ_a .

The results of these preliminary simulations are very promising. $\tau_a = 0.4$ in the computations is actually a rather large aerosol optical thickness in a realistic situation. Usually, the aerosol optical thickness τ_a over the oceans is $\lesssim 0.2$,²⁷ and the CZCS-observed Angström exponent n_a was usually ~ 0 . For a small aerosol optical thickness the error $\Delta\rho(\lambda_1)$ is qualitatively similar to larger aerosol optical thicknesses, but quantitatively smaller. The simulations suggest that in a typical situation the error in the retrieved water-leaving reflectance will usually be $\lesssim 0.0005$ using the proposed atmospheric correction algorithm, given knowledge of the surface roughness. This is 5-10 times smaller than the error in the standard CZCS correction algorithm.

A Possible Implementation of the Algorithm

In a realistic situation, the sun angle (θ_0) and the viewing angle (θ, ϕ) can assume the following values: usually, θ_0 is from $0^\circ \sim 80^\circ$, θ is from $0^\circ \sim 50^\circ$ and $45^\circ \lesssim \phi \lesssim 135^\circ$. It is difficult to have tables of $S(\lambda)$ and $I(\lambda)$ available for all these angles on an image processing system. Particularly, it would be very inconvenient if they had to be stored for all values of the angle ϕ . To reduce storage, we expand $S(\lambda)$ and $I(\lambda)$ in a Fourier series in ϕ and store only the Fourier coefficients. $S(\lambda)$ and $I(\lambda)$ for any ϕ can then be obtained easily. The radiance L at the top of the atmosphere is an even function of the azimuth angle ϕ . $\rho_t - \rho_r$ and ρ_{as} are also even functions of ϕ . Therefore, $S(\lambda)$ and

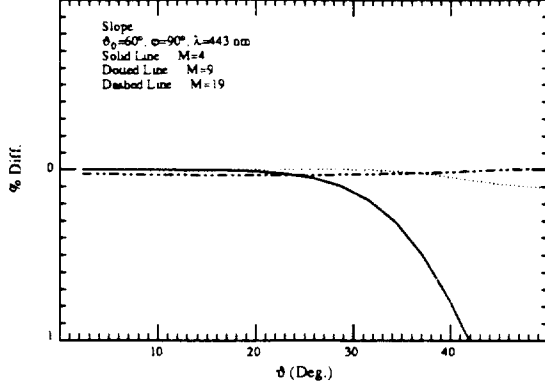


Figure 19. % difference of slope as a function of the viewing angle for $\theta_0 = 60^\circ$, $\phi = 90^\circ$ and $\lambda = 443$ nm. The solid line is for the Fourier order $M = 4$, dotted line is for $M = 9$, and dashed line is for $M = 19$.

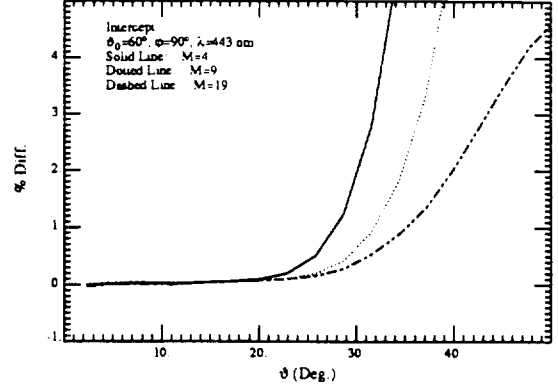


Figure 20. % difference of intercept as a function of the viewing angle for $\theta_0 = 60^\circ$, $\phi = 90^\circ$ and $\lambda = 443$ nm. The solid line is for the Fourier order $M = 4$, dotted line is for $M = 9$, and dashed line is for $M = 19$.

$I(\lambda)$ are even functions of ϕ , and we can write

$$S(\theta, \theta_0, \sigma, \lambda, \phi) = S^{(0)}(\theta, \theta_0, \sigma, \lambda) + 2 \sum_{m=1}^M S^{(m)}(\theta, \theta_0, \sigma, \lambda) \cos m(\phi - \phi_0), \quad (12)$$

$$I(\theta, \theta_0, \sigma, \lambda, \phi) = I^{(0)}(\theta, \theta_0, \sigma, \lambda) + 2 \sum_{m=1}^M I^{(m)}(\theta, \theta_0, \sigma, \lambda) \cos m(\phi - \phi_0), \quad (13)$$

or

$$S^{(m)}(\theta, \theta_0, \sigma, \lambda) = \frac{1}{\pi} \int_0^\pi S(\theta, \theta_0, \sigma, \lambda, \phi) \cos m(\phi - \phi_0) d\phi, \quad (14)$$

$$I^{(m)}(\theta, \theta_0, \sigma, \lambda) = \frac{1}{\pi} \int_0^\pi I(\theta, \theta_0, \sigma, \lambda, \phi) \cos m(\phi - \phi_0) d\phi. \quad (15)$$

These two integrals must be calculated numerically. Figures 19-20 give examples of % difference between true slope and intercept and the slope and intercept computed using different numbers of Fourier orders (M) in the case of $\theta_0 = 60^\circ$, $\phi = 90^\circ$ and $\lambda = 443$ nm. The x-axis in the figure is the viewing angle up to 50° . Note that the correct value of slope is much more important in the new algorithm than the intercept since the intercept is usually very small. Obviously, the results are quite good. The error of the slope is $\lesssim 0.1\%$ up to 50° for $M = 9$, and the error of intercept is $\lesssim 5\%$ up to 40° for $M = 9$. The error $\Delta\rho(\lambda_1)$ for all the cases considered in the previous section has been re-calculated by using the Fourier series for S and I with $M = 9$ and it is virtually identical to the original results.

Conclusion

The Rayleigh-aerosol interaction term ρ_{ra} is very difficult to model in a realistic situation. However, the combination of the Rayleigh-aerosol interaction term, ρ_{ra} , and the reflectance due to the aerosol alone, ρ_a , can be retrieved very accurately using the proposed atmospheric correction algorithm. The new algorithm is based on the facts that (1) there exists a near-linear relationship between $\rho_a + \rho_{ra}$ and ρ_{as} , and (2) a similarity in the distribution of points $(\rho_a + \rho_{ra}, \rho_{as})$ around the least-squares line for different wavelengths. From the simulations, it appears that for realistic situations the error in the retrieved water-leaving reflectance should be within the allowed limits for SeaWiFS for $\theta_0 \lesssim 60^\circ$. However, this error could be outside acceptable limits in some situations if the sea surface roughness is unknown. Thus, it is desirable that the wind speed be estimated for the process of atmospheric correction. The knowledge of vertical structure of the atmosphere does not appear to be as important as the surface roughness. The error in using the incorrect assumption for the vertical structure was found to be small. Therefore the two-layer model with molecules (Rayleigh scattering) above the aerosols for the air-sea system appears to be a reasonable model to use in the simulations for the future planned ocean color sensors. It is not necessary to use the ERTE in the computation of $S(\lambda)$ and $I(\lambda)$ for SeaWiFS, since the ρ_w can be retrieved with sufficient accuracy using the values computed from scalar theory. Although, this will introduce some error, a significant saving in computation time is achieved. However, in the case of instruments with higher radiometric sensitivity than SeaWiFS, e.g., MODIS, it may be necessary to use vector theory for the computation of S and I . To apply the new algorithm, the variation of the Ozone optical thickness (τ_{O_2}) and atmospheric pressure must be estimated, (either from other sensors and/or models), since errors in these quantities may lead to additional errors in ρ_w that will exceed the allowable limit.²⁸ Finally, it must be pointed out that the influence of whitecaps^{29,30} has been ignored. Whitecaps will add a constant (nonspectral) background to ρ_w (~ 0.001 for wind speed of 7.5 m/s), which will be interpreted as aerosol by an atmospheric correction algorithm. The influence of whitecaps on the proposed algorithm is under study.

References

- [1] W. A. Hovis, D. K. Clark, F. Anderson, R. W. Austin, W. H. Wilson, E. T. Baker, D. Ball, H. R. Gordon, J. L. Mueller, S. Y. E. Sayed, B. Strum, R. C. Wrigley and C. S. Yentsch, "Nimbus 7 coastal zone color scanner: system description and initial imagery," *Science* **210**, 60-63 (1980).
- [2] H. R. Gordon, D. K. Clark, J. L. Mueller and W. A. Hovis, "Phytoplankton pigments derived from the Nimbus-7 CZCS: initial comparisons with surface measurements," *Science* **210**, 63-66 (1980).
- [3] H. R. Gordon and A. Y. Morel, *Remote Assessment of Ocean Color for Interpretation of Satellite Visible Imagery: A Review* (Springer-Verlag, New York, 1983), 114 pp.
- [4] NASA and the Earth Observations Satellite Company, *System Concept for Wide-Field-of-View Observations of Ocean Phenomena from Space* (August 1987).
- [5] NASA, *MODIS (Moderate-Resolution Imaging Spectrometer), Earth Observing System Volume IIb* (1986).
- [6] NASA, *Earth Observing System (Eos) Background Information Package, Announcement of Opportunity No. OSSA-1-88* (Announcement of Opportunity No. OSSA-1-88, January 1988).
- [7] H. R. Gordon, "Radiative Transfer: A Technique for Simulating the Ocean in Satellite Remote Sensing Calculations," *Applied Optics* **15**, 1974-1979 (1976).
- [8] H. R. Gordon, "Removal of Atmospheric Effects from Satellite Imagery of the Oceans," *Applied Optics* **17**, 1631-1636 (1978).

- [9] H. R. Gordon and D. K. Clark, "Atmospheric effects in the remote sensing of phytoplankton pigments," *Boundary-Layer Meteorology* **18**, 299–313 (1980).
- [10] H. R. Gordon, D. K. Clark, J. W. Brown, O. B. Brown, R. H. Evans and W. W. Broenkow, "Phytoplankton pigment concentrations in the Middle Atlantic Bight: comparison between ship determinations and Coastal Zone Color Scanner estimates," *Applied Optics* **22**, 20–36 (1983).
- [11] M. Viollier, D. Tanre and P. Y. Deschamps, "An algorithm for remote sensing of water color from space," *Boundary Layer Meteorology* **18**, 247–267 (1980).
- [12] H. R. Gordon and D. J. Castaño, "The Coastal Zone Color Scanner Atmospheric Correction Algorithm: Multiple Scattering Effects," *Applied Optics* **26**, 2111–2122 (1987).
- [13] H. R. Gordon, J. W. Brown and R. H. Evans, "Exact Rayleigh Scattering Calculations for use with the Nimbus-7 Coastal Zone Color Scanner," *Applied Optics* **27**, 862–871 (1988).
- [14] H. R. Gordon and M. Wang, "*Surface Roughness Considerations for Atmospheric Correction of Ocean Color Sensors. 1: The Rayleigh Scattering Component*," 1991, Submitted to *Applied Optics*.
- [15] H. R. Gordon and M. Wang, "*Surface Roughness Considerations for Atmospheric Correction of Ocean Color Sensors. 2: Error in the Retrieved Water-leaving Radiance*," 1991, Submitted to *Applied Optics*.
- [16] H. R. Gordon and D. J. Castaño, "Aerosol Analysis with the Coastal Zone Color Scanner: A Simple Method for Including Multiple Scattering Effects," *Applied Optics* **28**, 1320–1326 (1989).

- [17] P. Y. Deschamps, M. Herman and D. Tanre, "Modeling of the atmospheric effects and its application to the remote sensing of ocean color," *Applied Optics* **22**, 3751-3758 (1983).
- [18] H. R. Gordon and D. K. Clark, "Clear water radiances for atmospheric correction of coastal zone color scanner imagery," *Applied Optics* **20**, 4175-4180 (1981).
- [19] C. Cox and W. Munk, "Measurements of the Roughness of the Sea Surface from Photographs of the Sun's Glitter," *Jour. Opt. Soc. of Am.* **44**, 838-850 (1954).
- [20] T. Nakajima and M. Tanaka, "Effect of Wind-Generated Waves on the Transfer of Solar Radiation in the Atmosphere-Ocean System," *Jour. Quant. Spectr. Rad. Trans.* **29**, 521-537 (1983).
- [21] E. L. Dereniak and D. G. Crowe, *Optical Radiation Detectors* (Wiley, New York, 1984), 300 pp.
- [22] H. Quenzel and M. Kastner, "Optical properties of the atmosphere: calculated variability and application to satellite remote sensing of phytoplankton," *Applied Optics* **19**, 1338-1344 (1980).
- [23] D. Deirmendjian, *Electromagnetic Scattering on Spherical Polydispersions* (Elsevier, New York, NY, 1969), 290 pp.
- [24] G. W. Kattawar, "A three-parameter analytic phase function for multiple scattering calculations," *J. Quant. Spectrosc. Radiat. Transfer* **15**, 839-849 (1975).
- [25] The concentration of phytoplankton pigment, C , is the sum of the concentrations of chlorophyll- a and phaeophytin- a .

- [26] G. W. Kattawar, G. N. Plass and S. J. Hitzfelder, "Multiple scattered radiation emerging from Rayleigh and continental haze layers. 1: Radiance, polarization, and neutral points," *Applied Optics* **15**, 632-647 (1976).

- [27] P. J. Reddy, F. W. Kreiner, J. J. Deluisi and Y. Kim, "Aerosol Optical Depths Over the Atlantic Derived From Shipboard Sunphotometer Observations During the 1988 Global Change Expedition," *Global Biogeochemical Cycles* **4**, 225-240 (1990).

- [28] J. -M. André and A. Morel, "Simulated Effects of Barometric Pressure and Ozone Content Upon the Estimate of Marine Phytoplankton From Space," *Jour. Geophys. Res.* **94C**, 1029-1037 (1989).

- [29] H. R. Gordon and M. M. Jacobs, "Albedo of the Ocean-Atmosphere System: Influence of Sea Foam," *Applied Optics* **16**, 2257-2260 (1977).

- [30] P. Koepke, "Effective Reflectance of Oceanic Whitecaps," *Applied Optics* **23**, 1816-1824 (1984).

Figure Captions

Figure 1. $NE\Delta\rho$ as a function of θ_0 at the scan edge for SeaWiFS. The solid and dotted lines are, respectively, for $p = 0.5$ and $p = 1.0$.

Figure 2. Aerosol phase functions used in the study: Dotted line, Haze L; Dashed line, Haze C; Solid line, Marine aerosol model.

Figure 3. $\rho_a + \rho_{ra}$ as a function of ρ_{as} for $\theta_0 = 60^\circ$, $\theta = 45.25^\circ$, and $\phi = 90^\circ$ at $\lambda = 665$ nm.

Figure 4. $\rho_a + \rho_{ra}$ as a function of ρ_{as} for $\theta_0 = 60^\circ$, $\theta = 45.25^\circ$, and $\phi = 90^\circ$ at $\lambda = 565$ nm.

Figure 5. $\rho_a + \rho_{ra}$ as a function of ρ_{as} for $\theta_0 = 60^\circ$, $\theta = 45.25^\circ$, and $\phi = 90^\circ$ at $\lambda = 443$ nm.

Figure 6. Error in the retrieved reflectance at the scan edge as a function of the sun angle for a Marine aerosol with $\tau_a(\lambda_4) = 0.4$ and $n_a = 0$. The surface roughness is unknown.

Figure 7. Error in the retrieved reflectance at the scan edge as a function of the sun angle for a Marine aerosol with $\tau_a(\lambda_4) = 0.4$ and $n_a = 0$. The surface roughness is known.

Figure 8. Error in the retrieved reflectance at the scan edge as a function of the sun angle for a Haze L aerosol with $\tau_a(\lambda_4) = 0.4$ and $n_a = 0$. The surface roughness is known.

Figure 9. Error in the retrieved reflectance at the scan edge as a function of the sun angle for a Haze C aerosol with $\tau_a(\lambda_4) = 0.4$ and $n_a = 0$. The surface roughness is known.

Figure 10. Error in the retrieved reflectance at the scan edge as a function of the sun angle for a Marine aerosol with $\tau_a(\lambda_4) = 0.4$ and $n_a = 0$. The surface roughness is known, but the vertical structure of atmosphere is unknown.

Figure 11. Error in the retrieved reflectance at the scan edge as a function of the sun angle for a Haze L aerosol with $\tau_a(\lambda_4) = 0.4$ and $n_a = 0$. The surface roughness is known, but the vertical structure of atmosphere is unknown.

Figure 12. Error in the retrieved reflectance at the scan edge as a function of the sun angle for a Haze C aerosol with $\tau_a(\lambda_4) = 0.4$ and $n_a = 0$. The surface roughness is known, but the vertical structure of atmosphere is unknown.

Figure 13. Error in the retrieved reflectance at the scan edge as a function of the sun angle for a Marine aerosol with $\tau_a(\lambda_4) = 0.2$ and $n_a = 1$. The surface roughness is known.

Figure 14. Error in the retrieved reflectance at the scan edge as a function of the sun angle for a Haze L aerosol with $\tau_a(\lambda_4) = 0.2$ and $n_a = 1$. The surface roughness is known.

Figure 15. Error in the retrieved reflectance at the scan edge as a function of the sun angle for a Haze C aerosol with $\tau_a(\lambda_4) = 0.2$ and $n_a = 1$. The surface roughness is known.

Figure 16a. P_{11} element of the scattering matrix for aerosols (solid line) and molecules (dotted line) as a function of the scattering angle. $P_{22} = P_{11}$.

Figure 16b. P_{12} element of the scattering matrix for aerosols (solid line) and $-P_{12}$ for molecules (dotted line) as a function of the scattering angle. $P_{21} = P_{12}$.

Figure 16c. P_{33} element of the scattering matrix for aerosols (solid line) and molecules (dotted line) as a function of the scattering angle. $P_{44} = P_{33}$.

Figure 16d. P_{34} element of the scattering matrix for aerosols (solid line) and molecules ($P_{34} = 0$) as a function of the scattering angle. $P_{43} = -P_{34}$.

Figure 17. Error in the retrieved reflectance including polarization at the scan edge as a function of the sun angle for $\tau_a(\lambda_4) = 0.2$ and $n_a = 0$. The surface roughness is known.

Figure 18. Error in the retrieved reflectance including polarization at the scan edge as a function of the sun angle for $\tau_a(\lambda_4) = 0.4$ and $n_a = 0$. The surface roughness is known.

Figure 19. % difference of slope as a function of the viewing angle for $\theta_0 = 60^\circ$, $\phi = 90^\circ$ and $\lambda = 443$ nm. The solid line is for the Fourier order $M = 4$, dotted line is for $M = 9$, and dashed

line is for $M = 19$.

Figure 20. % difference of intercept as a function of the viewing angle for $\theta_0 = 60^\circ$, $\phi = 90^\circ$ and $\lambda = 443$ nm. The solid line is for the Fourier order $M = 4$, dotted line is for $M = 9$, and dashed line is for $M = 19$.